



Universiteit  
Leiden  
The Netherlands

## **T-CYCLE EPR Development at 275 GHz for the study of reaction kinetics & intermediates**

Panarelli, E.G.

### **Citation**

Panarelli, E. G. (2018, December 10). *T-CYCLE EPR Development at 275 GHz for the study of reaction kinetics & intermediates*. *Casimir PhD Series*. Retrieved from <https://hdl.handle.net/1887/68233>

Version: Not Applicable (or Unknown)

License: [Licence agreement concerning inclusion of doctoral thesis in the Institutional Repository of the University of Leiden](#)

Downloaded from: <https://hdl.handle.net/1887/68233>

**Note:** To cite this publication please use the final published version (if applicable).

Cover Page



Universiteit Leiden



The handle <http://hdl.handle.net/1887/68233> holds various files of this Leiden University dissertation.

**Author:** Panarelli, E.G.

**Title:** T-CYCLE EPR Development at 275 GHz for the study of reaction kinetics & intermediates

**Issue Date:** 2018-12-10

**1**

# **Introduction**

## 1.1 Motivation and scope

Over the past century, scientific breakthroughs whose contributors were bestowed with a Nobel prize have been achieved in a wide range of fields thanks to studies related to chemical kinetics. In biochemistry, for instance, fundamental chemical kinetics investigations allowed to unravel the biocatalytical role of RNA [1], and to shed light on the mechanisms of protein degradation [2], of DNA repair [3], and of the synthesis of ATP [4] [5]. In inorganic chemistry, important studies clarified, for instance, the adsorption of gases on solid surfaces [6] [7], the mechanism of certain chain reactions [8], the mechanism of formation and decomposition of ozone [9], the dynamics of chemical elementary processes [10], and molecular dynamics on the femtosecond time scale [11].

Given the wealth of information that can be derived from chemical kinetics, it is important to develop methodologies for detection of reactive species with adequate time resolution. Coupling kinetic information with structural information opens the doors to understanding the mechanisms and functions of reactive (bio)chemical systems. This thesis is devoted to the development of methods for kinetic investigations (Rapid Freeze-Quench and Temperature-Cycle), coupled with the spectroscopic technique of choice for structural investigations of paramagnetic spin systems, namely Electron Paramagnetic Resonance, particularly at high magnetic field [12].

In this introductory Chapter the necessary background is provided to understand the research described in this thesis. First, the grounds of the theory of chemical kinetics are outlined, which allow the qualitative and quantitative interpretation of chemical reactivity. Following, an overview is given on Rapid Freeze-Quench, one of the most widespread methods to freeze reaction intermediates for spectroscopic characterization. Next, an alternative method to investigate chemical reactions is introduced. Finally, the theory and applications are presented of Electron Paramagnetic Resonance, the spectroscopic technique used for the kinetic investigations throughout this research.

## 1.2 Chemical kinetics

The study of the kinetics of reactive chemical species can give important insights in the understanding of the mechanism and function of a dynamical chemical system. In enzymatic reactions, for example, knowing about the reaction mechanism may unravel the entire functioning of proteins and their relations with the more complex biological contexts they operate in. As the main subject of this thesis is, in broad sense, the development of a method to qualitatively and quantitatively study reactive chemical systems, ample use has been made of concepts deriving from

## 1. INTRODUCTION

---

the theory of chemical kinetics, whose principles are briefly described hereinafter. Way more complete descriptions can be found in textbooks, like [13].

A chemical reaction is characterized by its *velocity*, namely the rate at which reactants are depleted and products are generated, defined by the so-called *rate law* of a reaction. A simple and generic chemical reaction may be written as follows:



where A and B are two reactants, which react to yield a product P.  $c_A$ ,  $c_B$ , and  $c_P$  are the stoichiometric coefficients of A, B, and P, respectively. The velocity  $v(t)$  at which A and B are depleted, or P is formed, defines the rate law of the reaction, and can be written as Equation 1.2:

$$v(t) = -\frac{1}{c_A} \frac{d[A]}{dt} = -\frac{1}{c_B} \frac{d[B]}{dt} = +\frac{1}{c_P} \frac{d[P]}{dt} \quad (1.2)$$

where  $[A]$ ,  $[B]$ , and  $[P]$  are the concentrations (in mol per volume unit) of species A, B, and P, respectively. The negative sign indicates the depletion of the reagents, while the positive sign indicates the generation of the product.

Experimentally, the rate law can be related to the concentration of the reagents through a proportionality constant  $k$ , called *rate constant*. Equation 1.2 can thus also be written as:

$$v(t) = k[A]^a[B]^b \quad (1.3)$$

where  $k$  is the rate constant of the reaction, and  $a$  and  $b$  are coefficients whose sum expresses the *order of reaction*, and commonly takes on the values of 0, 1, 2, or half-integer numbers. It is important to notice that the value of  $k$ , as well as the order of reaction, are properties that can only be determined experimentally.

Bimolecular reactions of the kind expressed by Equation 1.1 are often of second order, meaning that the coefficients  $a$  and  $b$  are equal to 1 and their sum is 2. Determining the rate constant of a second-order reaction is possible by adjusting the experimental conditions such that one of the two reactants (say B) is present in excess concentration as compared to the other. When  $[B] \gg [A]$ , the concentration of B does not change significantly in time, so that it can be approximated to a constant, and be included in the rate constant. Equation 1.3 can thus be written as:

$$k[A][B] \cong k'[A] \quad (1.4)$$

where  $k' = k[B]$  is the *apparent* rate constant. From Equations 1.2, 1.3, and 1.4, the dependence of the concentration of one reactant on time can be expressed analytically:

$$\frac{d[A]}{dt} = -k'[A] \quad (1.5)$$

where the stoichiometric coefficient  $c_A$  was set, for simplicity, to 1. Since the form of Equation 1.5 resembles the rate law of a first-order reaction, such conditions are called of *pseudo-first order*. By integrating Equation 1.5, the resulting dependence of  $[A]$  on time turns out to be exponential:

$$[A]_t = [A]_0 e^{-k't} \quad (1.6)$$

where  $[A]_t$  and  $[A]_0$  are, respectively, the concentration of reagent A at time  $t$ , and the initial concentration of reagent A. It is clear from Equation 1.6 that operating under pseudo-first-order conditions is an advantage when studying the kinetics of a chemical reaction, because the concentration dependence of one single reactant as a function of time takes the form of a simple exponential and can be easily linearized. Pseudo-first-order conditions were used in Chapters 2 and 4 of this thesis.

In spite of its name, a rate constant is not really constant, because it depends on several physical conditions of the reacting system, most importantly the temperature. An empirical relation between  $k$  and  $T$  was found by the Swedish scientist Svante Arrhenius [14], after whom the following equation takes its name:

$$k(T) = \mathcal{A} e^{-\frac{E_a}{RT}} \quad (1.7)$$

where  $\mathcal{A}$  is a constant called pre-exponential factor,  $E_a$  is the *activation energy* of the reaction (which is an inherent property of the reaction and does not depend on temperature), and  $R$  is the universal gas constant. The Arrhenius equation is found to be valid for many reactions; however, there exist variations on such an equation that plug in additional terms (for instance, a temperature-dependent pre-exponential factor) to account for deviations of some reactions from the simple Arrhenius behaviour. The activation energy featuring in Equation 1.7 represents the kinetic barrier the reactants have to go through in order to reach the so-called transition state,

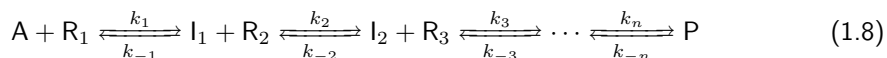
## 1. INTRODUCTION

---

which evolves into the product [15]. Thermodynamic formulations of the Arrhenius equation, such as the Eyring equation [16], correlate the activation energy to the Gibbs energy of activation, which contains the activation enthalpy used to define whether a reaction is endo- or exothermic. When the activation enthalpy is positive, the reaction is called *endothermic*, as it requires energy to progress, and the rate constant increases as a function of temperature. On the contrary, when the activation enthalpy is negative, the reaction is *exothermic*, meaning it releases energy as heat as it progresses, and the rate constant decreases as a function of temperature.

Equation 1.7 can be used to plot the logarithm of  $k$  versus  $\frac{1}{T}$  (known as Arrhenius plot) to find the activation energy when the behaviour of  $k$  as a function of  $T$  is known. Use of the Arrhenius plot is made in the analysis of Chapter 4 of this thesis.

Many chemical reactions, like virtually all enzymatic reactions, do not occur in one single step that turns the reagent(s) directly to the product(s). Rather, several intermediate steps take place, each one of them producing a transient species that serves as the reagent for the next step. A chemical reaction can thus be conceived as a sequence of *elementary reactions*, each defined by a rate constant  $k_j$  and an intermediate species  $I_j$ :



where  $A$  is the initial reagent,  $R_j$  are the reactive species involved in each step, and  $P$  is the final product. The  $R_j$ 's are not necessarily present, as the intermediates  $I_j$  might evolve spontaneously to the next product. In principle each elementary reaction may or may not be in chemical equilibrium (indicated by the double arrows), characterized by a forward rate constant ( $k_j$ ) and a backward rate constant ( $k_{-j}$ ).

An important feature of the reaction intermediates is their transient nature. Reaction intermediates tend to be energetically unstable, so that their conversion towards the products is highly favourable and fast [17]. For this reason, their concentration during the reaction peaks well before the reaction is complete. Also, their concentration tends to be much lower than that of the reagent(s) and the product(s), given the high rate of conversion to the product(s). The typical concentration profile as a function of time of an intermediate of a first-order reaction can be seen in Figure 1.1, where, as the concentration of reagent  $A$  (in red) decreases exponentially and the product  $P$  (in blue) is generated, the intermediate  $I$  (in green) peaks at some point during the reaction, and then fades away upon completion of the reaction. A great many (bio)chemical reactions occur in short time scales (e.g., in milliseconds), like those under study in Chapter 2, 4, and 5 of this thesis. The reaction intermediates of such reactions are therefore not easy

to detect, as the time they exist during the reaction is extremely short, and their usually low concentration does not help detecting them. For this reason, several techniques have emerged to address the problem of intermediate detection.

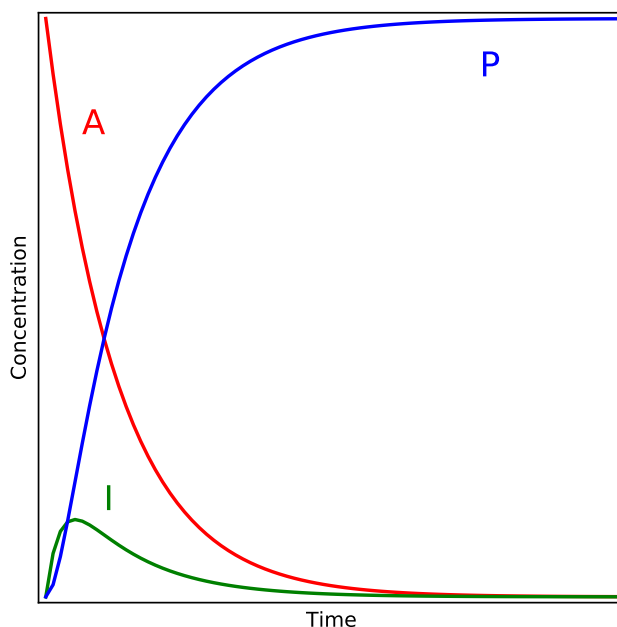


Figure 1.1: Concentration profiles of the species involved in a simple first-order reaction of the kind  $A \xrightarrow{k_1} I \xrightarrow{k_2} P$ , with A being the reagent (plotted in red), I the intermediate (plotted in green), and P the product (plotted in blue). Notice that in this example no equilibrium is considered in between the elementary reactions. Furthermore, the second elementary reaction, generating the product from the intermediate, is faster than the first elementary reaction, being  $k_2 = 5k_1$ .

### 1.3 Rapid Freeze-Quench

One of the most commonly used techniques to trap reaction intermediates on time scales of milliseconds is the so-called Rapid Freeze-Quench (RFQ), first implemented by Bray in 1961 [18] and in use ever since. Owing to the relatively high time resolution of this technique (down to milliseconds), and to the possibility to couple it to several spectroscopic detection methods, RFQ has been improved over the years and widely employed in combination with Electron Paramagnetic

## 1. INTRODUCTION

---

Resonance (EPR). Chapter 2 of this thesis is devoted to the coupling of RFQ to high-frequency EPR, and many details are provided there. Here, a brief introduction to the principles of RFQ is provided.

RFQ consists of the rapid reaction quench of a mixture of two or more chemically reactive samples, caused by the mixture's fast freezing in a cryogenic bath. Prior to the freezing, the reagents have first rapidly and homogeneously mixed and then reacted for a well-defined amount of time. In the setup used for the experiments of Chapter 2 of this thesis, the two reactants (here labeled A and B) are contained in two separate syringes that are mounted on a stage coupled to a ram. The ram is connected to a console-controlled servo motor that can move the ram upwards, thereby pushing the pistons of the syringes symmetrically and injecting equal volumes of the solutions of reactants to the mixer, to which the syringes are connected by suitable plastic tubes. The mixer is specifically designed to rapidly and homogeneously mix the two reactant solutions before injecting them to a so-called *aging tube*, whose length is one of the parameters that determine the reaction time ( $t_r$ ) of the mixture. At the end of the aging tube is a nozzle that sprays the mixture into a cryogenic bath (most commonly isopentane at a temperature of about 140 K). The cold medium immediately freezes the droplets of mixture, thereby quenching the reaction at a specific  $t_r$ . The frozen droplets take the shape of particles that can be collected in a sample holder for later measurements. Specifically in this thesis (see Chapter 2), the RFQ particles were collected in EPR tubes and later transferred into smaller capillaries suitable for high-frequency EPR.

In the RFQ setup used in Chapter 2, three parameters can be directly set in the ram-controlling console, which will determine the *reaction time* of the mixture for a given length of the aging tube. These parameters are:

- the *ram velocity*  $U_R$  (between 0.8 and 8 cm s<sup>-1</sup>), which is the actual velocity of the ram;
- the *total displacement*  $d_T$  (between 0.01 and 10 cm per experiment), which is the length by which the ram moves per experiment;
- the *delay factor*, which sets one or more incubation times between consecutive ram displacements.

For the RFQ experiment designed in Chapter 2, only the first two settings were taken into account. In what follows is shown how the ram velocity and the total displacement directly affect the *flow rate* of the mixture pushed by the pistons through the syringes to the mixer and the

aging tube. The flow rate in turn affects the reaction time, which is the time the mixture spends in the aging tube, and thus the time amount by which the reaction has progressed. Notice that the following equations were derived from [19], whose notation is reproduced here.

The flow rate (in mL s<sup>-1</sup>) is described by the continuity equation relating the ram velocity (directly set from the console) and the flow velocity in the aging tube:

$$Q = A_s U_R = A_r U_x \quad (1.9)$$

where  $A_s$  is the cross-sectional area of the syringe (in cm<sup>2</sup>),  $U_R$  is the ram velocity (in cm s<sup>-1</sup>),  $A_r$  is the cross-sectional area of the aging tube (in cm<sup>2</sup>), and  $U_x$  is the flow velocity in the aging tube (in cm s<sup>-1</sup>). Since the cross-sectional area of the syringe is related to the total volume of the syringe, being  $V_s = A_s d_T$ , it results from Equation 1.9 that  $Q = \frac{V_s}{d_T} U_R$ , which indicates that the flow rate is directly determined by the console-controlled ram velocity and total displacement.

Since the flow velocity in the aging tube can be expressed as  $U_x = l_r/t_r$ , the numerator being the length of the aging tube and the denominator being the time the mixture spends in the reaction tube (or reaction time), through Equation 1.9 it is possible to express the reaction time as:

$$t_r = \frac{l_r}{U_x} = \frac{A_r l_r}{A_s U_R} = \left( \frac{D_r}{D_s} \right)^2 \frac{l_r}{U_R} \quad (1.10)$$

where  $D_r$  and  $D_s$  are the diameters of the aging tube and of the syringe, respectively. In the experiments described in Chapter 2 of this thesis, they have values of 0.05 cm and 0.7 cm, respectively, while the ram velocity is set to 3.2 cm s<sup>-1</sup>. In this way, once the console parameters are set, and the syringe volume and the aging tube diameter are known, Equation 1.10 allows to calculate the reaction time per RFQ experiment only as a function of the length of the aging tube.

A final important remark concerns the so-called *dead time* or – as is called in Chapter 2 – the *freezing time* of the RFQ setup. Owing to the connections between the tubes, the syringes, and the mixer, any RFQ setup has an intrinsic *dead volume* that is filled by the mixture during the freezing time, which adds up to the actual reaction time. The temporal outcome of a RFQ experiment is thus expressed in terms of an overall non-consistently defined *aging time* [20] or *quenching time* [21], which has to be corrected by the freezing time (determined experimentally) when performing quantitative kinetic studies with RFQ.

### 1.4 Laser-induced Temperature-jumps

The laser-induced Temperature-jump (T-jump) methodology was originally developed to study the relaxation of (bio)chemical systems in equilibrium, following the perturbation of the equilibrium induced by a heat source (such as an electrical discharge [22] or a near-infrared (NIR) laser pulse [23]), which causes the system to quickly reach a higher temperature before going back to the initial temperature after the heat source is turned off. Particularly in the case of a laser-induced T-jump, the absorption of the NIR energy, typically by the solvent molecules (e.g., water), results in the heating of the sample volume, with a temperature difference ( $\Delta T$ ) that depends on:

- the heat conductivity and heat capacity of the solvent and sample holder;
- the optical intensity of the laser pulse;
- the optical absorption of the solvent molecules at a specific excitation wavelength.

In this thesis, a laser-induced T-jump methodology was developed, in combination with high-frequency Electron Paramagnetic Resonance (hence named T-Cycle EPR), for the investigation of reaction kinetics between two chemically reactive species. The T-jump method developed here has similarities with the one employed for relaxation studies. However, the important difference with T-jump relaxation methodologies is that T-Cycle EPR involves the application of T-jumps on a system that does not feature any chemical equilibrium, i.e., a frozen mixture of reactants where no reaction is taking place. As such, the method is thus not developed with the aim of observing the relaxation of the system back to its equilibrium state following a laser-induced T-jump. Rather, the jumps applied here serve as "heating shots" that warm up the system to a temperature where a chemical reaction can take place for a certain amount of time, to which follows the return of the system to a frozen state where no reaction occurs. This allows the observation of the step-wise progress of a chemical reaction as a function of time, with no focus whatsoever as regards the relaxation of the system.

An important aspect of the sample heating with a laser pulse for kinetic studies is that it should take place homogeneously over the whole sample volume, so as to ensure a single, well-defined reaction temperature of the sample – this being the equilibrium temperature between two opposing driving forces, namely the heating by the laser pulse, and the cooling by the thermal bath. To this end, a small sample volume is paramount, in order to maximize the rate of heat transfer. This is one of the reasons why the T-jump methodology developed here was coupled

to high-frequency EPR, which makes use of relatively small sample volumes. Evidence of the homogenous heating produced by the laser pulses used in the setup of T-Cycle EPR described in this thesis is given in Figure 1.2, where the 275 GHz cw EPR spectra of a solution of TEMPOL in a mixture of water and glycerol are shown as a function of the nominal laser power. To record these spectra, the laser was turned on continuously, and a spectrum was recorded for different laser powers, in increasing order. These spectra can be easily interpreted and simulated by taking into account one single spectral component (as described in the Appendix to Chapter 3), which implies they are not the summation of many different spectra that originate from zones of the sample at different temperatures. The homogenous heating of the sample produced by the laser-induced T-jumps applied here is facilitated by the small sample volume (about 20 nL), and is in agreement with what has been reported by Azarkh and Groenen in [24].

A key point to achieve fast and homogenous T-jumps is the efficient absorption of the NIR energy by the solvent molecules. Water has a broad absorption in its NIR spectrum peaking around 1450 nm, originating from the first overtone of the O—H bond stretching [25]. The absorption coefficients at 1600 nm (i.e., about the wavelength of the laser used in Chapters 3 to 5, at 1550 nm) of pure water [26], pure glycerol [27], and mixtures of water and glycerol 1:1 in volume [27] are, respectively, 7.7, 11.6, and 9.8 cm<sup>-1</sup>. In particular, the mixture of water and glycerol has an absorption increased by roughly 25% as compared to that of pure water, an observation in agreement with the work by Azarkh and Groenen [24].

## 1.5 Electron Paramagnetic Resonance

Electron Paramagnetic Resonance (EPR) is a powerful spectroscopic technique useful for structural investigations of paramagnetic species such as organic radicals, metal ions, or defect centres in solids. Similarly to the more common Nuclear Magnetic Resonance (NMR), where radio-frequency-induced nuclear spin transitions are measured, in EPR microwave-induced transitions between electron spin energy levels are detected. Since the energy of the spin levels of an electron are very sensitively influenced by its environment, valuable information can be extracted from an EPR spectrum when the quantum mechanical energy description of the electron – its spin Hamiltonian – is known. Nowadays, alongside the traditional continuous-wave (cw) approach in EPR, more and more sophisticated microwave pulse sequences are being developed to provide ever more detailed information on the spin systems of interest. Moreover, the technical achievements in microwave technology made EPR at higher microwave frequencies feasible, making it very accessible and widespread, allowing improved spectral resolution (both in EPR and Electron Nuclear Double Resonance spectra), a better identification of certain parameters of the

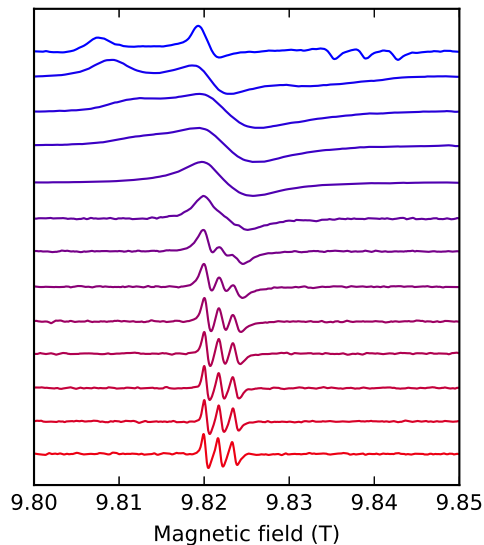


Figure 1.2: 275 GHz cw EPR spectra of TEMPOL, at a concentration of 1 mM, in solution with a mixture of water and glycerol 95:5 in volume. The spectra are recorded with the laser turned on continuously at increasing optical power (top blue @ 0.0 W, bottom red @ 2.0 W), from a cryostat temperature of -50 °C.

spin Hamiltonian (like the zero-field splitting), and a higher absolute sensitivity owing to a large Boltzmann factor [12], not to mention that in certain systems the only possibility to induce EPR transitions is with microwave quanta of high frequency. Hereinafter is a general introduction to the basic theory of EPR meant to understand the spin systems studied in this thesis. Complete treatments of the subject can be found, for instance, in [28] and [29].

### 1.5.1 The electron Zeeman effect and the $g$ -factor

To illustrate the principles of EPR, the simplest paramagnetic system is considered first, namely an isolated electron having a spin  $S = 1/2$ . When a particle with non-zero spin is subject to an externally applied magnetic field, the energy levels associated to its spin will split as a function of the magnetic field (Equation 1.11), a phenomenon first observed by the Dutch physicist Pieter Zeeman and thus called Zeeman effect. Quantum mechanically, energy levels resulting from such effect on an electron spin can be expressed with the following spin Hamiltonian ( $\mathcal{H}$ ):

$$\mathcal{H} = g_e \mu_B \mathbf{S} \cdot \mathbf{B} \quad (1.11)$$

where  $g_e = 2.0023$  is the  $g$ -factor of an isolated electron in the vacuum,  $\mu_B$  is the Bohr magneton,  $\mathbf{B}$  is the external magnetic field, and  $\mathbf{S}$  is the electron spin. Since  $\mathbf{B}$  is oriented along one direction (conventionally,  $z$ ), only the magnetic field magnitude  $B_0$  is taken into account, and therefore only the  $S_z$  component of the spin operator  $\mathbf{S}$ . In particular for the case of  $S = 1/2$ , the eigenvalues of  $S_z$  are  $m_S = \pm \frac{1}{2}$ , and the eigenvalues of the spin Hamiltonian of Equation 1.11 (namely, the energy levels of the electron spin) can be written as  $E_{\pm} = \pm \frac{1}{2} g_e \mu_B B_0$ , which evidences the dependence of the energy splitting on the external magnetic field.

The energy splitting of the spin levels is thus proportional to the magnitude of the external magnetic field, but also depends on the  $g$ -factor, a quantity that acts as a proportionality constant and is very sensitive to the magnetic environment of the electrons. In general, the  $g$ -factor is a tensorial entity,  $\mathbf{g}$ , and is called *anisotropic* when the diagonal components  $g_x$ ,  $g_y$ , and  $g_z$  of the matrix representation in the eigenbasis of  $\mathbf{g}$  are not equal. When this is the case, the splitting of the spin levels is different in different spatial directions, and the EPR transition arising from the spin Hamiltonian of Equation 1.11 will be observed at different values of the magnetic field, each one associated to a direction of  $\mathbf{g}$ .

To better illustrate the Zeeman effect and the influence of an anisotropic  $g$ -factor, in Figure 1.3 are plotted the spin levels of an  $S = 1/2$  system with a strongly anisotropic  $\mathbf{g}$  (as is the case for the system described in Chapter 5 of this thesis) as a function of the externally applied magnetic field. At zero field, the spin states are degenerate, and by increasing the magnitude of the external magnetic field, such states are split anisotropically and proportionally to  $g_x$  (red),  $g_y$  (green), or  $g_z$  (blue). When operating at 9.5 GHz (Figure 1.3 A), one of the most common frequencies in EPR, the three transitions (depicted as grey lines) associated to the three different values of  $\mathbf{g}$  are observed between roughly 300 and 350 mT. In particular, the two at higher field (corresponding to  $g_x$  and  $g_y$ ) are separated by about 5 mT. When going to higher magnetic field, a correspondingly higher microwave frequency is required to match the energy difference between the spin levels and induce an EPR transition. Figure 1.3 B shows such situation at the EPR frequency of 275 GHz, with the three transitions associated to the anisotropic  $\mathbf{g}$  spreading between about 8700 and 9600 mT, and the two at higher field separated by about 140 mT. This simple example highlights a fundamental advantage of high-frequency (HF) EPR versus low-frequency (LF) EPR, namely a better resolution in magnetic field even for slightly anisotropic  $g$ -factors.

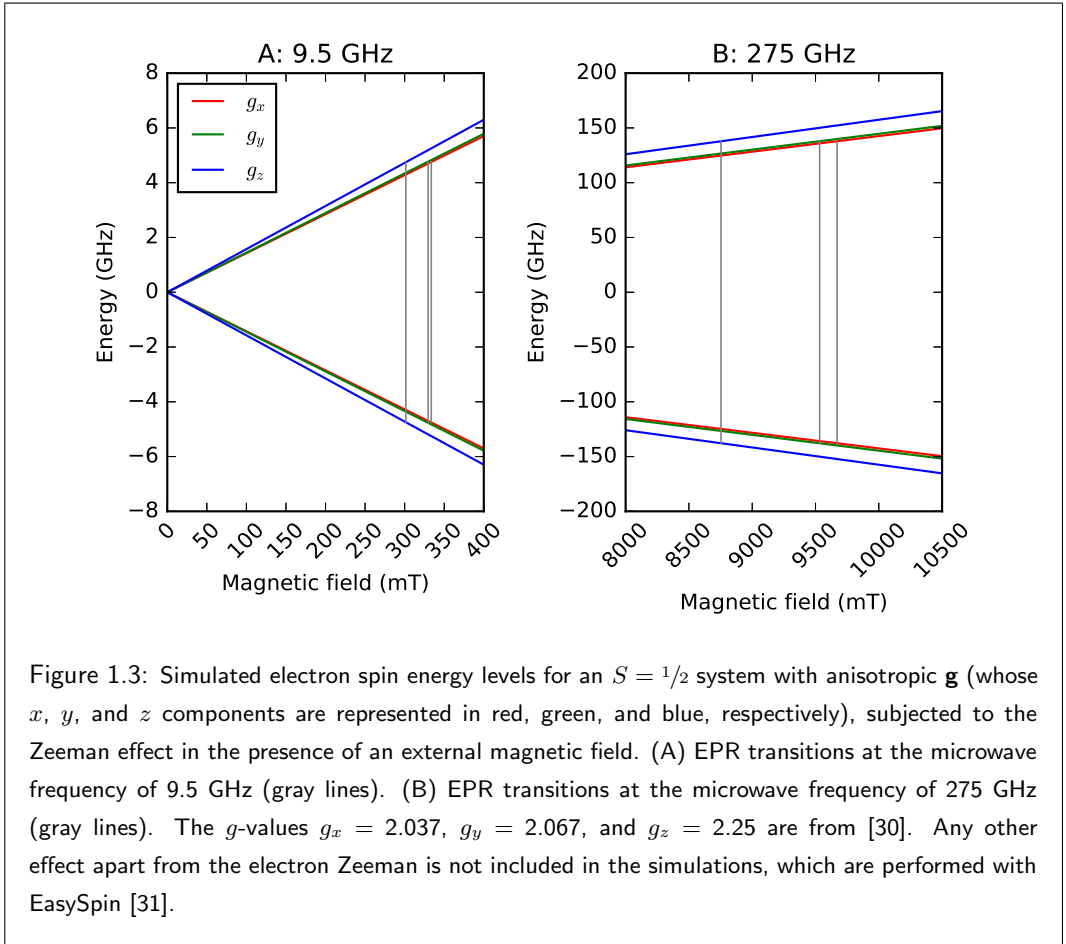


Figure 1.3: Simulated electron spin energy levels for an  $S = 1/2$  system with anisotropic  $g$  (whose  $x$ ,  $y$ , and  $z$  components are represented in red, green, and blue, respectively), subjected to the Zeeman effect in the presence of an external magnetic field. (A) EPR transitions at the microwave frequency of 9.5 GHz (gray lines). (B) EPR transitions at the microwave frequency of 275 GHz (gray lines). The  $g$ -values  $g_x = 2.037$ ,  $g_y = 2.067$ , and  $g_z = 2.25$  are from [30]. Any other effect apart from the electron Zeeman is not included in the simulations, which are performed with EasySpin [31].

### 1.5.2 Electron spin – nuclear spin interaction: the hyperfine coupling

One of the most interesting properties of spins is their ability to interact with each other. The interaction between electron spins and nuclear spins, called hyperfine coupling, provides a great deal of information about the chemical environment of an electron. In the general case where one electron with spin  $S = 1/2$  interacts with one nucleus with spin  $I$ , the resulting spin Hamiltonian can be expressed as:

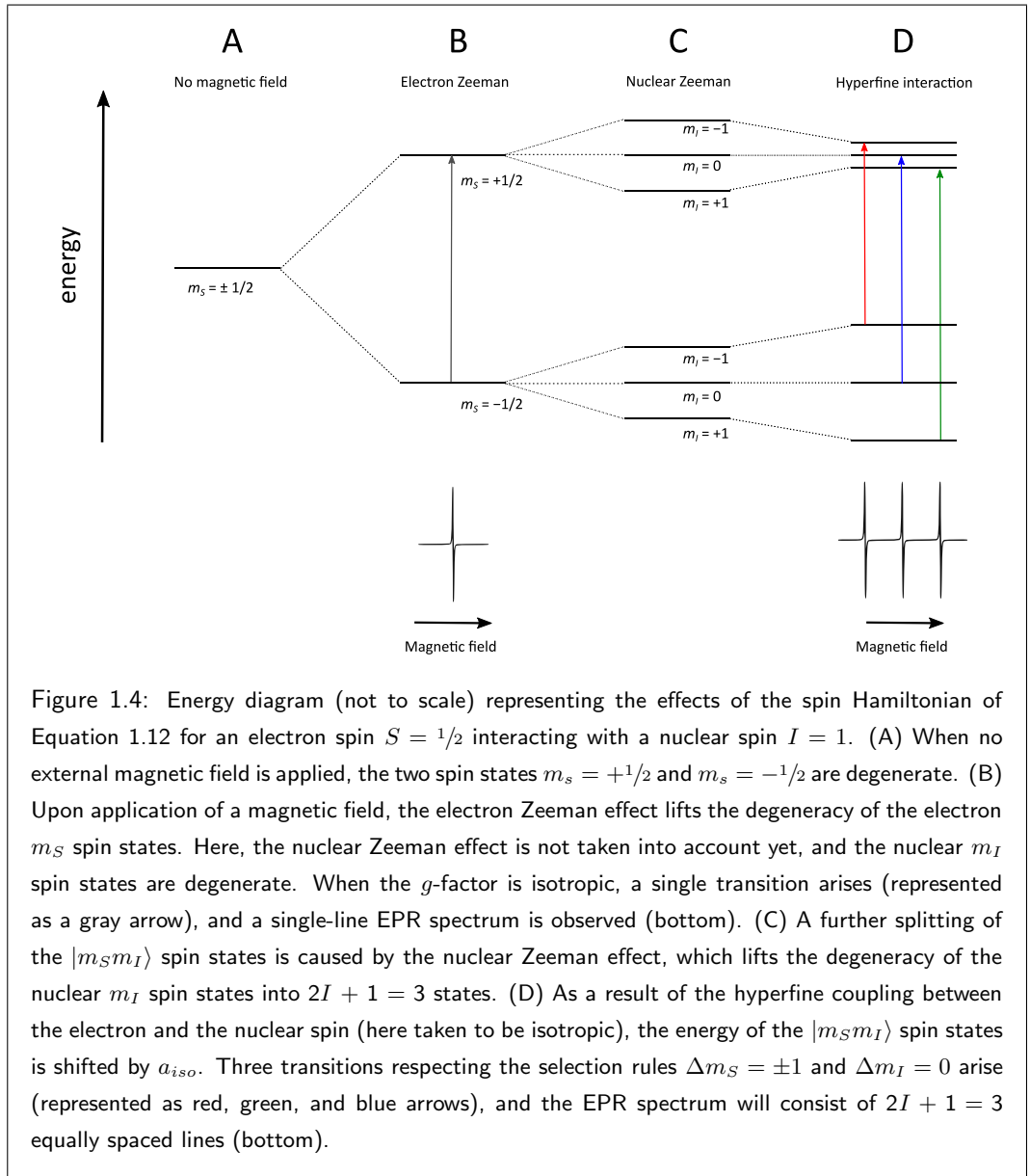
$$\mathcal{H} = g_e \mu_B \mathbf{S} \cdot \mathbf{B} - g_N \mu_N \mathbf{I} \cdot \mathbf{B} + \mathbf{S} \cdot \mathbf{A} \cdot \mathbf{I} \quad (1.12)$$

where the first term represents the electron Zeeman effect, the second term represents the nuclear Zeeman effect, and the third term represents the hyperfine interaction between the

electron spin and the nuclear spin. Like for the electron Zeeman term, also the nuclear Zeeman term contains a nuclear  $g$ -factor,  $g_N$ , and the nuclear magneton,  $\mu_N$ . The hyperfine interaction is represented by the tensor  $\mathbf{A}$ , which can be viewed as composed of an *isotropic* contribution and an *anisotropic* one (similarly to the  $\mathbf{g}$  tensor), namely  $\mathbf{A} = a_{iso} + \mathbf{T}$ .

The effect of the Zeeman term on the nuclear spin is similar to that on the electron spin, namely it splits the energy levels of the nuclear spin as a function of the external magnetic field. To understand how this works, Figure 1.4 schematically illustrates the energy splitting of a system composed of one electron spin  $S = 1/2$  with isotropic  $g$ -factor, interacting with one nuclear spin  $I = 1$  (such as that of  $^{14}\text{N}$ ). For simplicity, the terms of the spin Hamiltonian of Equation 1.12 are applied separately and sequentially in the scheme. When no external magnetic field is applied, all the energy levels of this  $S = 1/2 ; I = 1$  system are collapsed on one and are thus degenerate (A). Upon applying a magnetic field, the electron spin levels are subject to the Zeeman term (Figure 1.4 B) and are split according to the magnetic quantum numbers  $m_S = +1/2$  and  $m_S = -1/2$ , customarily labeled  $\alpha$  and  $\beta$ , respectively. Also the nuclear spin is subject to the Zeeman term (Figure 1.4 C), so that each of the  $\alpha$  and  $\beta$  states are further split according to the magnetic quantum number of the nuclear spin,  $m_I = +1$ ,  $m_I = 0$ , and  $m_I = -1$ . Lastly, the hyperfine coupling term applies on the aforesaid levels, shifting them by an amount defined by the hyperfine tensor  $\mathbf{A}$  (Figure 1.4 D). In the scheme of Figure 1.4, only the isotropic component ( $a_{iso}$ ) of the hyperfine coupling is taken into account. It can be appreciated how the single-line EPR signal arising from an isotropic  $g$ -factor and no hyperfine coupling (Figure 1.4 B, bottom) is split into  $2I + 1 = 3$  equally spaced lines (the spacing in magnetic field being proportional to  $a_{iso}$ ) as a result of the hyperfine interaction with the  $I = 1$  nucleus of  $^{14}\text{N}$  (Figure 1.4 D, bottom).

In real systems, it is often the case that both the hyperfine coupling *and* the  $g$ -factor are anisotropic. When the spectral resolution is not high enough, as in low-frequency EPR, it can be arduous to discern the various contributions of the  $\mathbf{A}$  and  $\mathbf{g}$  tensors on the EPR spectrum. At LF-EPR, such contributions might be hidden within the spectral linewidth, which is often broader than the magnitude of the hyperfine coupling itself, for instance. This can be visualized in Figure 1.5, where a spectral simulation is provided of a system such as a nitroxide radical (like TEMPOL, see Chapters 3 and 4), which features an unpaired electron with spin  $S = 1/2$  interacting with a  $^{14}\text{N}$  nucleus with spin  $I = 1$ . Both the  $g$ -factor and the hyperfine coupling are anisotropic, so that each of the three components of  $\mathbf{g}$  is split into  $2I + 1 = 3$  lines, for a total of in principle 9 lines. However, the 9.5 GHz spectrum of Figure 1.5 A shows a rather different situation, the reason for it being that both the splitting due to the  $g$ -factor and the



splitting due to the  $A_x$  and  $A_y$  components of  $\mathbf{A}$  are smaller than the spectral linewidth. The red and green dotted lines indicate the field positions of, respectively, the transitions associated to the  $g_x$  component and its  $A_x$  hyperfine component, and the transitions associated to the  $g_y$  component and its  $A_y$  hyperfine component. Only the  $A_z$  hyperfine component is large enough

to be discerned at 9.5 GHz, as shown by the peaks around 335 and 342 mT (the blue dotted line represents the field positions of such transitions). All the other transitions are hidden within the linewidth of the central peak around 339 mT, and cannot be resolved at the microwave frequency of 9.5 GHz. However, going to HF-EPR offers a much clearer picture of the system under study. In the spectrum of Figure 1.5 B, simulated for the microwave frequency of 275 GHz, the peaks associated to the three transitions arising from the anisotropic  $\mathbf{g}$  are clearly recognizable. The hyperfine splitting of the  $A_x$  and  $A_y$  components is still too small as compared to the spectral linewidth; however, the  $A_z$  component is large enough to give rise to three clearly separated lines of the  $g_z$  component around 9831, 9834, and 9837 mT. This example shows the advantages of high-frequency EPR over low-frequency EPR also in determining the hyperfine components of a paramagnetic system.

### 1.5.3 High-spin systems

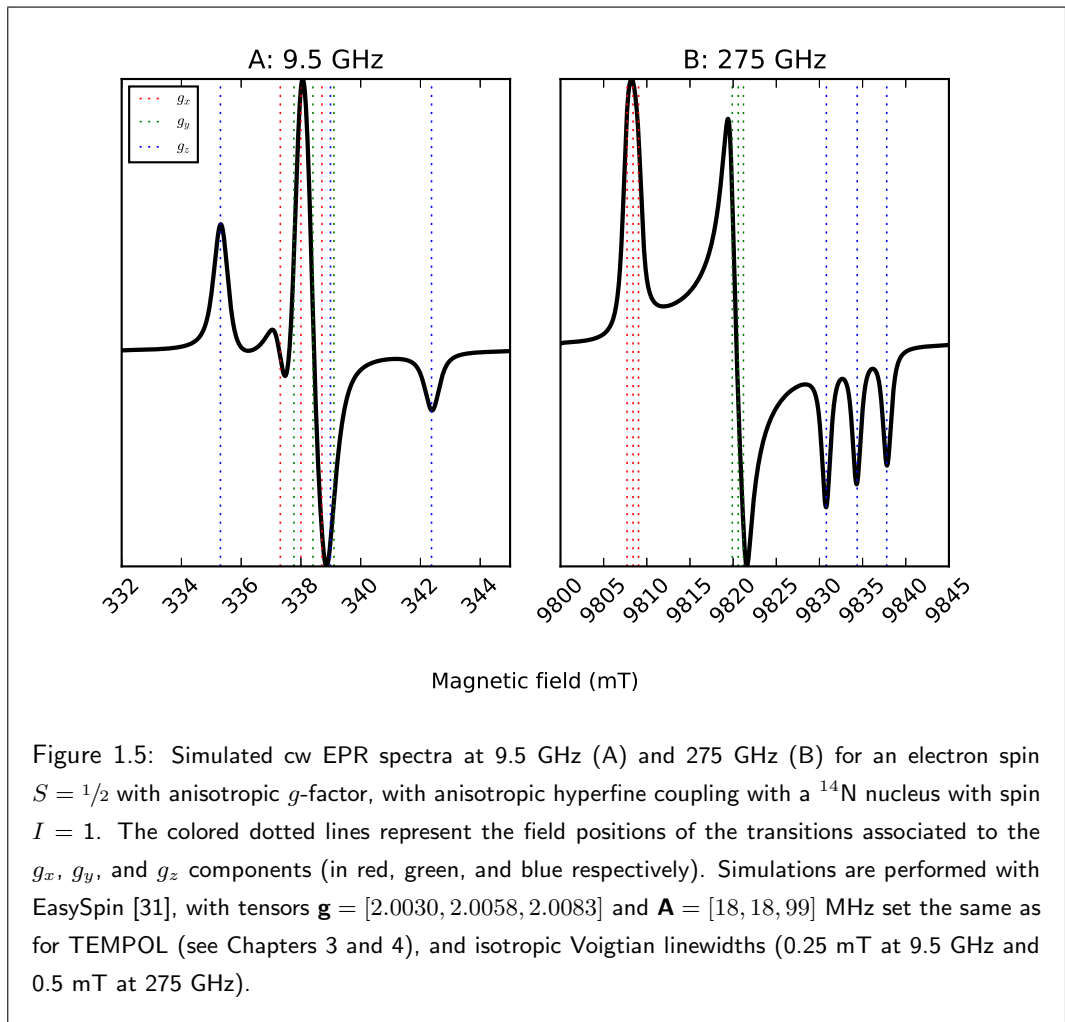
So far, only the case of a single unpaired electron with spin  $S = 1/2$  has been considered. However, it is fairly common to come across paramagnetic systems with spin higher than  $1/2$ , such as transition metal ions (like in Chapter 2), or several electron spins ferromagnetically coupled (like in Chapter 5).

In a high-spin system such as a transition metal ion, the unpaired electrons of the  $d$  (or  $f$ ) orbitals are subject to a second-order effect of the spin-orbit coupling known as zero-field splitting (ZFS), which is a term that adds to the system's spin Hamiltonian and takes the following form:

$$\mathcal{H}_{ZFS} = \mathbf{S} \cdot \mathbf{D} \cdot \mathbf{S} \quad (1.13)$$

where  $\mathbf{D}$  represents the zero-field splitting tensor. The name originates from the fact that such contribution does not depend on the external magnetic field, and an energy separation between the spin levels is present even in the absence of an externally applied magnetic field, being an intrinsic property of the system.

In Chapter 2 of this thesis, the paramagnetic system under study is a  $d^5$  Fe(III) center, which turns from a high-spin (HS)  $S = 5/2$  state to a low-spin (LS)  $S = 1/2$  state as a result of the replacement of its axial ligand, which induces a change in the strength of the crystal field. Figure 1.6 shows the zero-field splitting of the spin levels for HS-Fe(III). It can be noticed how, even in the absence of an external magnetic field ( $B_0 = 0$ ), the spin levels (arranged in degenerate spin multiplicities called Kramers doublets) are split by an amount proportional to  $\mathbf{D}$ . In this



case, the zero-field splitting tensor is isotropic, and so large ( $D = 315$  GHz [32]) that even at room temperature only the lowest Kramers doublet (corresponding to  $m_S \pm 1/2$ ) is populated, and only transitions between the  $m_S = +1/2 \leftrightarrow m_S = -1/2$  levels can be observed.

Systems with spin higher than  $1/2$  can also be the result of separate electron spins at a distance such that they can interact with each other. The electron–electron interaction consists of a classically-viewed dipolar contribution, and a quantum-mechanical *exchange* contribution:

$$\mathcal{H}_{12} = \mu_B(\mathbf{S}_1 \cdot \mathbf{g}_1 \cdot \mathbf{B} + \mathbf{S}_2 \cdot \mathbf{g}_2 \cdot \mathbf{B}) + \mathbf{S}_1 \cdot \mathbf{D}_{12} \cdot \mathbf{S}_2 - J_{12}\mathbf{S}_1 \cdot \mathbf{S}_2 \quad (1.14)$$

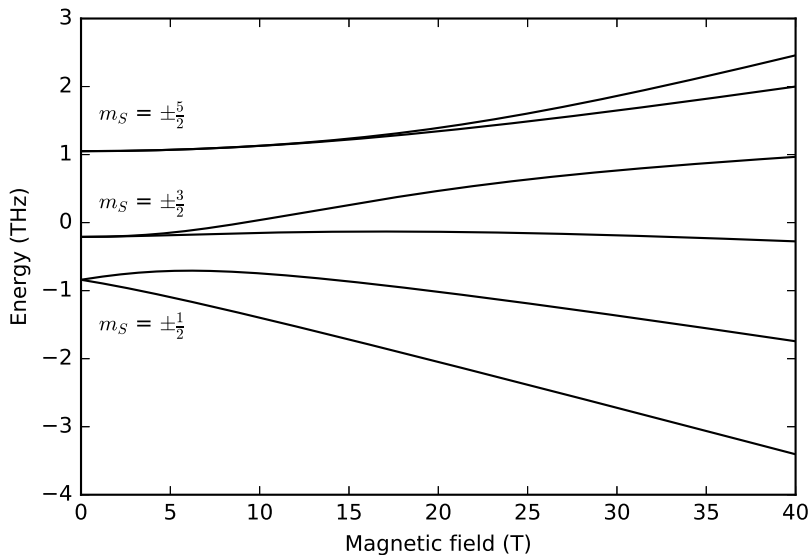
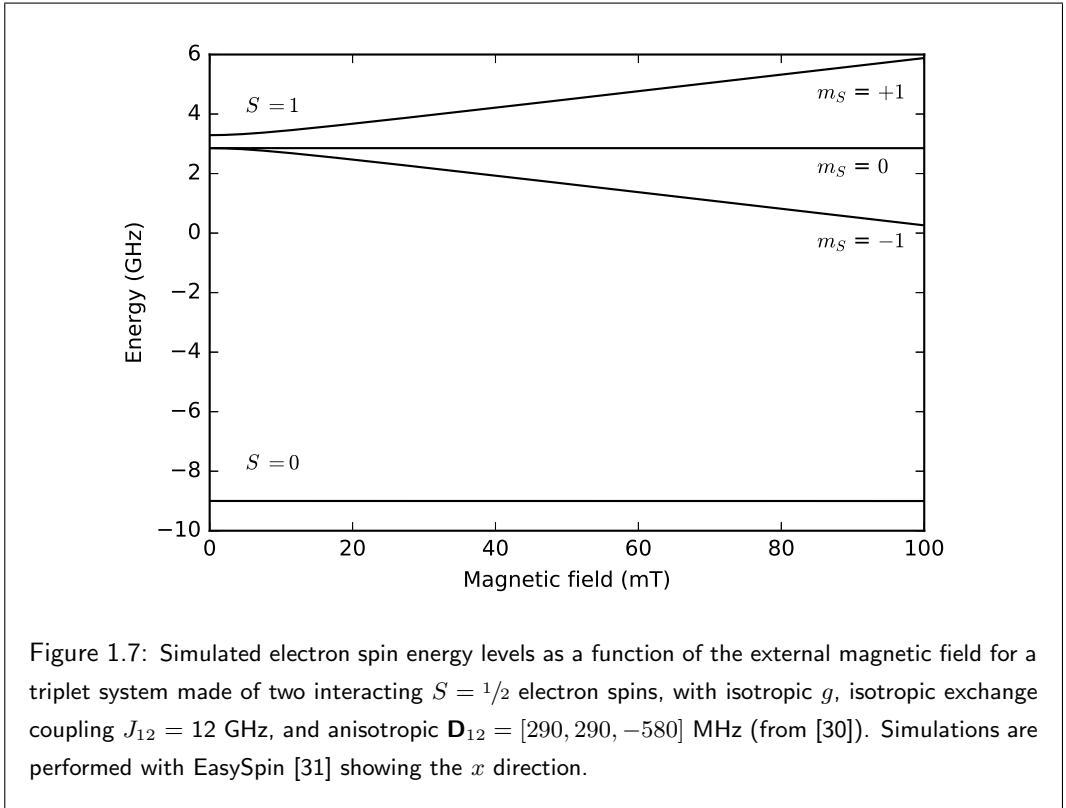


Figure 1.6: Simulated electron spin energy levels as a function of the external magnetic field for an  $S = 5/2$  system with isotropic  $g$  and isotropic  $D = 315$  THz (from [32]). Simulations are performed with EasySpin [31] showing the  $x$  direction.

where, in analogy to Equation 1.11, the first term is the electron Zeeman effect, the second term is the dipolar coupling between the two electrons ( $\mathbf{D}_{12}$  being the dipolar coupling tensor), and the third term is the exchange interaction between the two electrons ( $J_{12}$  being the isotropic exchange coupling). The subscripts refer to electron 1 or 2.

In Chapter 5 of this thesis, the paramagnetic intermediate of the enzyme under study is suggested to be a triplet system composed of a  $\text{Cu}^{2+}$  ion interacting with a tyrosyl radical (an organic radical), both with spin  $S = 1/2$ . Figure 1.7 shows the diagram of the magnetic field dependence of the spin levels of a simplified system, namely one where the  $g$ -factor is isotropic and there is no hyperfine interaction with the spin of the copper nucleus. As a result of the interaction of two spins  $S = 1/2$ , an  $S = 0$  and an  $S = 1$  spin multiplicity are generated (named singlet and triplet, respectively), whose energy separation is proportional to the exchange coupling  $J_{12}$ . The  $m_S = 1$  state of the  $S = 1$  spin multiplicity is further split from the  $m_S = 0$  and  $m_S = -1$  states by the dipolar coupling tensor  $\mathbf{D}_{12}$  at zero field. Transitions are possible only within the  $S = 1$  spin state, and not between the  $S = 0$  and the  $S = 1$  spin state.



EPR transitions are called "allowed" when they occur between spin levels with selection rule  $\Delta m_S = \pm 1$ . However, at LF-EPR, weaker transitions arise, called "forbidden", that deviate from the aforementioned selection rule and, in the case of a triplet state, occur between spin levels with  $\Delta m_S = \pm 2$ . These transitions, also called *half-field* transitions, occur when the Zeeman terms of the spin Hamiltonians of Equations 1.13 and 1.14 (which are field-dependent) are small in comparison to the ZFS or spin-spin interaction terms – in other words, when the external magnetic field is low or, equivalently, when the EPR microwave frequency is low. Under such circumstances, the spin levels are not well-defined by single magnetic quantum numbers, but rather are a mix of them. The abundance of half-field transitions at LF-EPR makes the resulting spectra extremely hard if not impossible to interpret, especially with systems with spin  $S > 1$ . However, the spin levels of such systems are "well-behaved" at high magnetic field, namely when the Zeeman terms are bigger than the ZFS or spin-spin interaction terms, meaning that the single spin levels can be correctly described by their magnetic quantum numbers, and no "forbidden" transitions occur. For this reason, HF-EPR is particularly suited for the study

and interpretation of high-spin systems.

#### 1.5.4 Slow-to-fast motion and rigid limit in EPR spectra

All the EPR spectra shown thus far originate from samples in the so-called *rigid limit*, namely samples whose paramagnetic species are not free to quickly rotate in any direction – a situation proper of solids. When this is the case, the paramagnetic species in a solid matrix are bound to a specific direction, and so are their electron spins. Such a rigid system is susceptible to the orientation of the external magnetic field as compared to the orientations of its own spin-Hamiltonian parameters, and the anisotropy (when present) is observable in the EPR spectra. In particular, powders and frozen solutions (i.e., disordered glasses) can be seen as ensembles of spins ranging all possible spatial directions – as opposed to single crystals, which have all of their spins oriented in the same direction, thus giving rise to EPR spectra associated to one specific spatial orientation. When the EPR spectrum of a powder is recorded (hence also called *powder spectrum*), the spin transitions of all possible orientations are induced, and a continuous absorption is measured. In practice, however, the resulting powder spectrum does not look like a continuous absorption as a result of the field modulation employed to record the spectrum, which causes it to appear like a first-derivative spectrum. All the spectral simulations shown before correspond to powder spectra.

The complete opposite case as that of a powder spectrum is when the paramagnetic species are freely rotating in their medium, a situation that normally occurs with molecules in solutions, and that is referred to as *fast motion*. Due to the fast rotational motion (or "tumbling") of the paramagnetic species in the solution, all the anisotropic terms of the system's spin Hamiltonian average out. What is thus visible in the EPR spectrum of a paramagnetic species in a solution is the mean value of the  $\mathbf{g}$  tensor and the isotropic component ( $a_{iso}$ ) of the hyperfine  $\mathbf{A}$  tensor. The components of the  $\mathbf{D}$  tensor average to zero in the fast-motion regime and the zero-field splitting is thus not measurable.

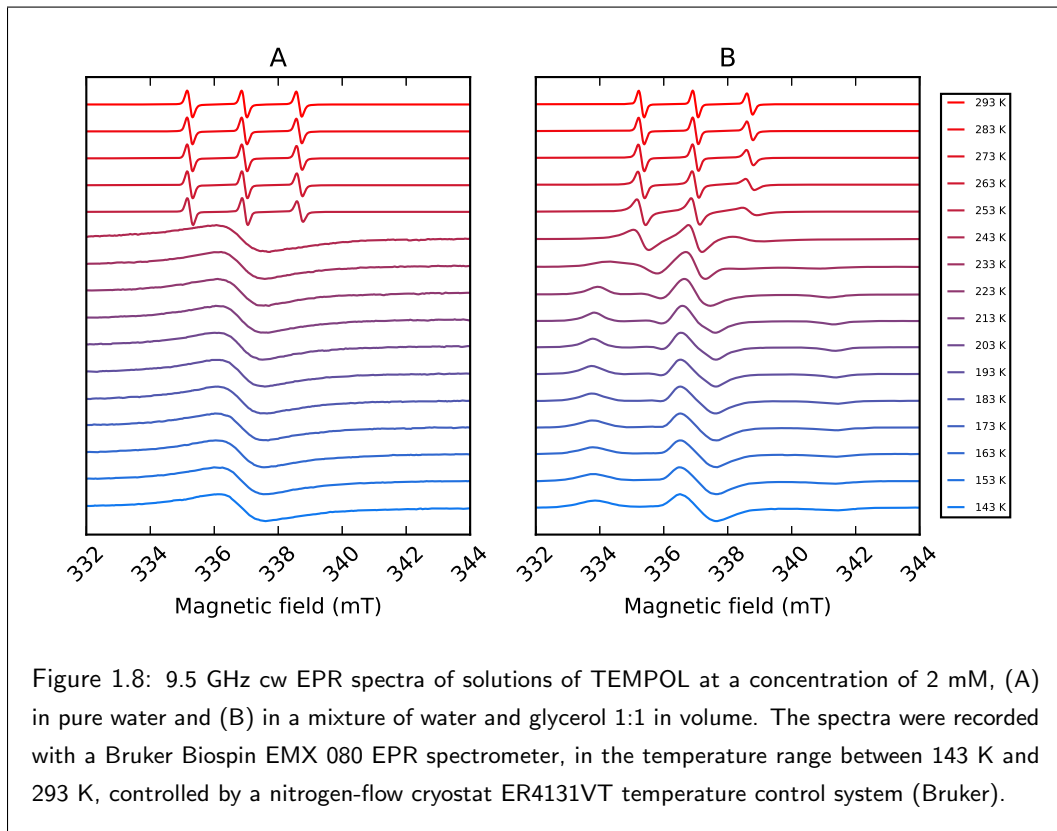
An intermediate situation between the rigid-limit and the fast-motion regimes also exists, namely when the medium containing the electron spins still allows rotational motion of the paramagnetic species, but such motion is hindered by physical factors such as the high viscosity of the solution (which is the case for the mixtures of water and glycerol described in Chapters 3 and 4) or steric effects (such as a spin label attached to a protein). As a result of these hindrance effects, the rotational motion of the paramagnetic species is slowed down or, equivalently, their *rotational correlation time* ( $\tau_c$ ) becomes longer, which affects the spin relaxation processes and the spectral line shapes [33]. The time  $\tau_c$  is defined as the average time in which a molecule

## 1. INTRODUCTION

---

rotates by one radian in a certain spatial direction, and it ranges from picoseconds for the fast-motional regime, to nanoseconds up to microseconds for the slow-motional regime. There are several models to describe such slow-motion effects (like the Stokes-Einstein equation used in the Appendix to Chapter 3 of this thesis), through which valuable information on the surroundings of a spin system can be obtained, such as the temperature of a solution, or the conformation of a spin-labeled protein.

Nitroxide radicals such as TEMPOL exhibit important changes of the spectral line shape as a function of their rotational correlation time. This is shown, as an example, in Figure 1.8, where the spectral linewidth changes of solutions of TEMPOL are plotted as a function of the sample temperature (in the range between 143 K and 293 K). A different dependence of the solution's viscosity on temperature affects the spectral shapes differently, so that a solution of TEMPOL in pure water (A), and a solution of TEMPOL in a mixture of water and glycerol 1:1 in volume (B) behave very differently as a function of temperature. Since the viscosity of liquid water does not change much with temperature, the mobility of the molecules in the solution is fast and roughly constant. This can be seen in the spectra of Figure 1.8 A in the temperature range from 293 K down to 253 K, where the spectral line shape does not change much. The three-line spectrum originates from the  $a_{iso}$  component of the hyperfine interaction of the electron with the  $^{14}\text{N}$  nucleus, as the anisotropic component is averaged to zero as a result of the fast rotational motion of the molecules in the solution. From 243 K down, the solution freezes and a powder spectrum arises, which has however an unusual shape. This is due to the fact the TEMPOL molecules, at a relatively high concentration, form clusters in the absence of glycerol in solution, becoming close enough to each other for their spins to interact intermolecularly, which results in a broadening of the line shape. Figure 1.8 B shows a rather different situation, because the viscosity of water and glycerol solutions varies greatly with temperature, affecting the rotational motion of the molecules and thus the spectral shape. A progressive spectral broadening is visible in the temperature range between 263 and 233 K, this being the range where the sample transitions from a fast-motion regime through a slow-motion regime, down to a rigid-limit regime. The plot of Figure 1.8 B highlights the importance of glycerol added to the solution, which has a "de-clustering" effect on the TEMPOL molecules. As a result, the changes in the spectral line shape of TEMPOL are easy to interpret and simulate, yielding information on the temperature of the solution (see Appendix to Chapter 3).



### 1.5.5 Home-built 275 GHz EPR spectrometer

The EPR spectra at the microwave frequency of 275 GHz described in this thesis were performed on a spectrometer built around 2000 by Blok and coworkers at Leiden University, and described in great detail by the same authors in [34]. The construction of such spectrometer was driven by ever-growing interest in HF-EPR, after spectrometers at frequencies such as 95 and 140 GHz became commercially available.

Here, a brief description of the setup is provided. A simplified block diagram of the home-built 275 GHz EPR spectrometer is shown in Figure 1.9, and consists of four main parts:

- (A) Two microwave sources, producing two microwave beams at the frequencies of 91.9 GHz and of 89.7 GHz, which are sent to diode triplers that return the frequencies of 275.7 GHz and 269.1 GHz. The former is the frequency used to excite the sample, while the latter serves as the local oscillator for the superheterodyne receiver.

## 1. INTRODUCTION

---

- (B) A microwave bridge operating in reflection mode, suitable for both cw and pulsed experiments. It transmits the incoming microwave frequencies to and from the resonant cavity with a quasi-optical transmission setup, which allows the confined beams of electromagnetic waves to travel in free space, thus making the transmission losses negligible – as opposed to conventional waveguide technologies at such high frequencies.
- (C) A single-mode, tunable resonant cavity which is located at the bottom of a variable-temperature helium-gas flow cryostat placed at the center of a superconducting magnet. The cavity is coupled to the microwave bridge through a corrugated circular waveguide whose geometry maximizes the microwave coupling and minimizes the transmission losses. The cavity has an absolute sensitivity as high as  $10^8$  spins per mT. The cylindrical cavity has a diameter of 1.4 mm and a length between 0.8 and 1.4 mm that can be varied with two plungers located at both sides, which move synchronously and symmetrically inward and outward so as to allow the tuning of the cavity. Underneath the cavity is a coil that generates the field modulation for cw experiments, and a grid that allows irradiation of the sample from an external source.
- (D) A superconducting solenoid magnet capable to reaching 14 T. The scan-to-scan field stability is less than 0.1 mT, while the day-to-day field stability is less than 1 mT.

The microwave beam reflected from the resonant cavity, carrying the EPR signal, is transmitted through the corrugated waveguide back to the bridge, where it reaches a Martin-Puplett diplexer, which combines the EPR signal at 275.7 GHz with the local oscillator at 269.1 GHz, giving both the same well-defined polarization. The coupled output signal is then directed to a polarization-sensitive microwave mixer where a signal is produced at the so-called intermediate frequency (IF) of  $275.7 - 269.1 = 6.6$  GHz. The IF signal is finally amplified and fed to a lock-in detector for cw experiments, or a boxcar integrator for pulsed experiments.

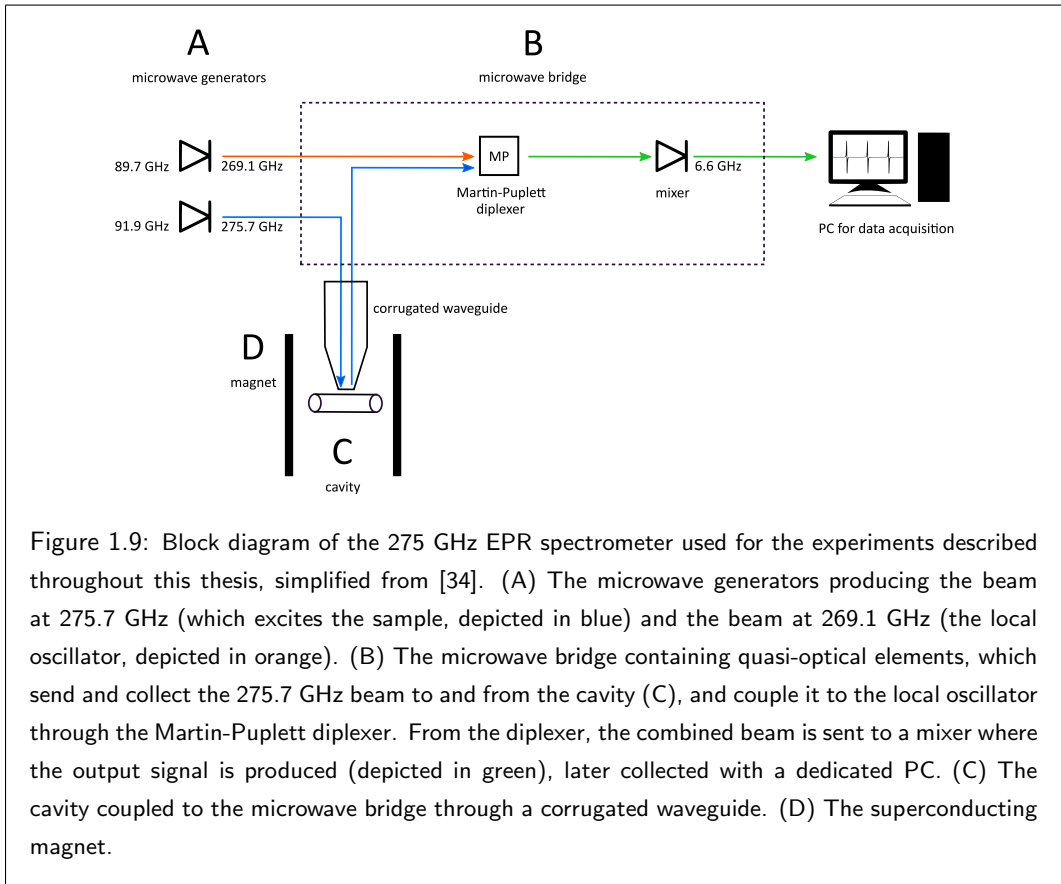


Figure 1.9: Block diagram of the 275 GHz EPR spectrometer used for the experiments described throughout this thesis, simplified from [34]. (A) The microwave generators producing the beam at 275.7 GHz (which excites the sample, depicted in blue) and the beam at 269.1 GHz (the local oscillator, depicted in orange). (B) The microwave bridge containing quasi-optical elements, which send and collect the 275.7 GHz beam to and from the cavity (C), and couple it to the local oscillator through the Martin-Puplett diplexer. From the diplexer, the combined beam is sent to a mixer where the output signal is produced (depicted in green), later collected with a dedicated PC. (C) The cavity coupled to the microwave bridge through a corrugated waveguide. (D) The superconducting magnet.



